

9 **Abstract**

10 We use model simulations and observations to examine how well the F10.7 and F30 solar radio
11 fluxes represent solar forcing in the thermosphere during the last 60 years of weakening solar
12 activity. We found that increased saturation of radio fluxes during the last two extended solar
13 minima leads to an overestimation of solar energy deposition, which manifests as a change in the
14 linear relation between thermospheric parameters and F10.7. On the other hand, the linear relation
15 between thermospheric parameters and F30 remains nearly the same throughout the whole studied
16 period because of a recently found relative increase of F30 with respect to F10.7. This explains the
17 earlier finding that F30 correlates better with several ionospheric and thermospheric parameters
18 than F10.7 during the last decades. We note that continued evaluation is needed to see how well
19 F10.7 and F30 will serve as solar proxies in the future when solar activity may start increasing
20 toward the next grand maximum.

21
22 **Short Summary**

23 We study how well the F10.7 and F30 solar radio fluxes represent solar energy input in the
24 thermosphere during the last 60 years. We found that increased saturation of radio fluxes at recent
25 solar minima leads to an overestimation of solar energy, which change the relation between
26 thermospheric parameters and F10.7, but this is not an issue for F30 because of a relative increase
27 of F30 with respect to F10.7. This explains why F30 has been found to represent solar energy
28 better than F10.7.

29
30 **1. Introduction**

31 The solar radio flux at 10.7 cm, F10.7, is a solar activity parameter which is widely used in
32 observational and modeling studies of the thermosphere and ionosphere, serving as a proxy of
33 solar extreme ultra-violet (EUV) irradiance in studies of space climate and space weather. For
34 example, it is used in the MSIS series of empirical models of the thermosphere (Emmert et al.,
35 2021 and references therein), and in the empirical solar irradiance EUVAC model (Richards et al.,
36 1994). EUVAC is widely used to parameterize solar spectral irradiance input in the upper
37 atmospheric general circulation models such as the Thermosphere-Ionosphere-Electrodynamics
38 General Circulation Model (TIE-GCM; Richmond et al., 1992, Qian et al., 2014), the
39 Thermosphere-Ionosphere-Mesosphere-Electrodynamics General Circulation Model (TIME-
40 GCM; Roble and Ridley, 1994), the Whole Atmosphere Community Climate Model with
41 thermosphere and ionosphere eXtension (WACCM-X; Liu et al., 2018), the Global Ionosphere
42 Thermosphere Model (GITM; Ridley et al., 2006), the Coupled Thermosphere Ionosphere
43 Plasmasphere electrodynamics model (CTIPe; Fuller-Rowell and Rees, 1980, Millward et al.,
44 2001), and the NOAA operational space weather forecast model, the Whole Atmosphere Model-
45 Ionosphere Plasmasphere Electrodynamics (WAM-IPE; T. J. Fuller-Rowell et al., 2008, Fang et
46 al., 2016, 2018) model.

47
48 However, some recent studies have suggested that the F30 flux, the solar radio flux at 30 cm,
49 is a better solar proxy than the F10.7 flux in representing the long-term solar EUV irradiance
50 impact in the thermosphere and ionosphere system. For example, using accelerometer data from
51 the Gravity field and steady-state Ocean Circulation Explorer (GOCE; November 2009–October
52 2013), the Gravity Recovery and Climate Experiment (GRACE, April 2003–December 2015), and
53 Stella (January 2000–April 2013), Dudok de Wit and Bruinsma (2017) found that the F30 flux
54 improves the response of the thermospheric density to solar forcing in the Drag Temperature

55 Model (DTM; Bruinsma et al., 2012, Bruinsma, 2015), with the model bias dropping on average
56 by 0–20% and the standard deviation of the bias being 15–40% smaller than when using the F10.7
57 flux. This improved performance is achieved for all three density datasets, covering both solar
58 cycle minimum and maximum conditions. In addition, based on analysis of changes in F2-layer
59 parameter data, several research groups have found that F30 is better than F10.7 in representing
60 F2 parameters. Using the ionospheric foF2 and foE parameters of four European stations with long
61 (1976–2014) data series, Lastovicka (2019) found that the dependence of yearly averaged values
62 of foF2 on F10.7 changed over time, being steeper in 1996–2014 than in 1976–1995. Using the
63 foF2 parameters of 11 ionospheric stations in four continents over 1976–2014, Laštovička &
64 Burešov (2023) further found that among the six studied solar activity proxies including sunspot
65 number, F10.7, F30, Mg II, He II, and H Lyman- α flux, the F30 flux is the best solar proxy to
66 explain the variability of foF2 at middle latitudes. In addition, the dependence of foF2 on F10.7
67 and sunspot number were found to be significantly steeper in 1996–2014 than in 1976–1995,
68 whereas the dependence of foF2 on F30 was the same in both intervals. Danilov and Berbeneva
69 [2024] also found that F30 is the best solar proxy to describe the seasonally dependent local-time
70 variation of foF2.

71
72 When studying the performance of F10.7 and F30 as solar EUV proxies in the thermosphere
73 and ionosphere, it is necessary to understand their origin and mutual relationship. Mursula et al.
74 (2024) analyzed solar radio flux observations from two independent observatories, the Penticton
75 (Canada) F10.7 flux, and four long-term radio fluxes from the Nobeyama National Astronomical
76 Observatory of Japan. They found that there is a systematic, long-term relative increase in all five
77 radio fluxes (originating in the upper chromosphere and low corona) with respect to the sunspot
78 number (photosphere) during the decay of the Modern Maximum from solar cycle 20 to solar cycle
79 24. Also, other chromospheric parameters like the MgII index were found to increase with respect
80 to sunspots. In addition, the fluxes of longer radio waves (from higher altitudes) were found to
81 increase with respect to the shorter radio waves (from lower altitudes). For example, F30 increased
82 relative to F10.7 during this period. Mursula et al. (2024) concluded that there is a relative
83 difference in the long-term evolution between the photosphere and the upper solar atmosphere
84 (chromosphere and low corona), as well as between different altitudes of the upper solar
85 atmosphere. This differential long-term evolution in the solar atmosphere due to the weakening
86 solar activity during the decay of the Modern Maximum may offer an explanation to why the F30
87 flux performs more consistently as a solar EUV proxy than the F10.7 flux. Note that the study
88 periods of those other recent studies mentioned above include the time when the largest relative
89 change between the different solar proxies was found by Mursula et al. (2024).

90
91 Considering the wide usage of the F10.7 flux in ionosphere-thermosphere (I-T) science, as well
92 as in space weather and space climate applications, it is imperative that we understand the long-
93 term evolution of the F10.7 flux and how well it really represents solar EUV forcing over multi-
94 decadal time scales. In this paper, we take an interdisciplinary approach to examine how well the
95 F10.7 and F30 fluxes represent solar EUV forcing in the thermosphere over multi-decadal time
96 scales when the highly active Modern Maximum (with the peak in cycle 19) was decaying to a
97 much lower activity level (~ 1961–2023). We will conduct this investigation using model
98 simulations of the upper atmosphere and analyzing related observational data.

99 100 **2. Model and Data**

101

102 *NCAR Global Mean Model*

103 The upper atmospheric model used in this study is a global mean version of the National Center
104 for Atmospheric Research (NCAR) TIME-GCM (Roble et al., 1987; Roble and Ridley, 1994;
105 Roble, 1995). Solar irradiance input (0–175 nm) and solar EUV energy deposition scheme is
106 described in Solomon and Qian (2005). Solar EUV spectral irradiance is based on the EUVAC
107 model, which is parameterized using the daily F10.7 value and the 81-day averaged value of F10.7
108 (Solomon and Qian, 2005). For simplicity, hereafter, we refer to the solar irradiance input in this
109 model as the EUVAC model.

110

111 We conducted two model runs under identical conditions, with one key difference: one run
112 utilized the actual observed F10.7 flux, while the other employed F30*, which is the F30 flux
113 scaled to the F10.7 level using the relation $F30^* = 1.554 \times F30 - 1.6$ (Dudok de Wit and Bruinsma,
114 2017). It's important to note that F30* retains the temporal variability of the F30 flux but aligns
115 with the magnitude of the F10.7 flux, allowing it to be used in the EUVAC model, which is based
116 on F10.7. Geomagnetic activity was kept constant at a relatively low level ($A_p = 4$) to eliminate
117 the influence of geomagnetic variability. Additionally, CO₂ concentrations were based on the same
118 time-varying measurements from the Mauna Loa Observatory (Qian et al., 2006) in both runs,
119 ensuring that the long-term thermospheric cooling due to increasing CO₂ concentration was
120 consistent in both model runs. Thus, the differences between the two runs stem from the use of
121 F10.7 versus F30*.

122

123 *Penticton F10.7 and Nobeyama F30 Radio Flux Data*

124 The NOAA F10.7 flux index covers the time from the start of continuous 10.7 cm
125 measurements (1947) until the end of April 2018, when the NOAA stopped the index production.
126 We continued the NOAA F10.7 flux from May 2018 onward using the recent Penticton radio flux
127 data available from the NRCan server, as described in more detail in Mursula (2023). NRCan
128 provides daily F10.7 flux from October 28, 2004 to present.

129

130 Continuous solar radio flux observations in Japan started in the early 1950s (Shimojo and Iwai,
131 2023). Observations are made at four frequencies (1, 2, 3.75, and 9.4 GHz; corresponding to
132 wavelengths 30 cm, 15 cm, 8 cm, and 3.2 cm, to be called F30, F15, F8 and F3.2) in Nobeyama,
133 Japan. Note that the observed daily solar radio fluxes are modulated by the level of solar activity
134 and by the changing distance between the Sun and the Earth due to eccentricity of the Earth's orbit.
135 Since the NCAR TIME-GCM considers solar irradiance variations due to the varying Sun-Earth
136 distance, the F10.7 and F30 fluxes presented in this paper and input to the model are adjusted radio
137 fluxes, which are the observed radio fluxes corrected for the varying Sun-Earth distance, given at
138 the fixed distance of one astronomical unit (AU). The unit of F10.7 and F30 is solar flux unit (sfu),
139 and $1 \text{ sfu} = 10^{-22} \text{ W m}^{-2} \text{ Hz}^{-1}$. Note that provisional solar radio flux data (with data quality flag=1)
140 are excluded in our data analysis.

141

142 *Satellite Drag Derived Thermospheric Mass Density*

143 Satellite drag derived thermospheric mass density dataset is a long-term data set of globally
144 averaged thermospheric mass density derived from orbit data of about 7,700 objects in a low-
145 Earth orbit, affected by atmospheric drag (Emmert et al., 2021). The data cover the years 1967–
146 2019 and altitudes 250–575 km. Temporal resolution is 3–4 days for most years. These data are

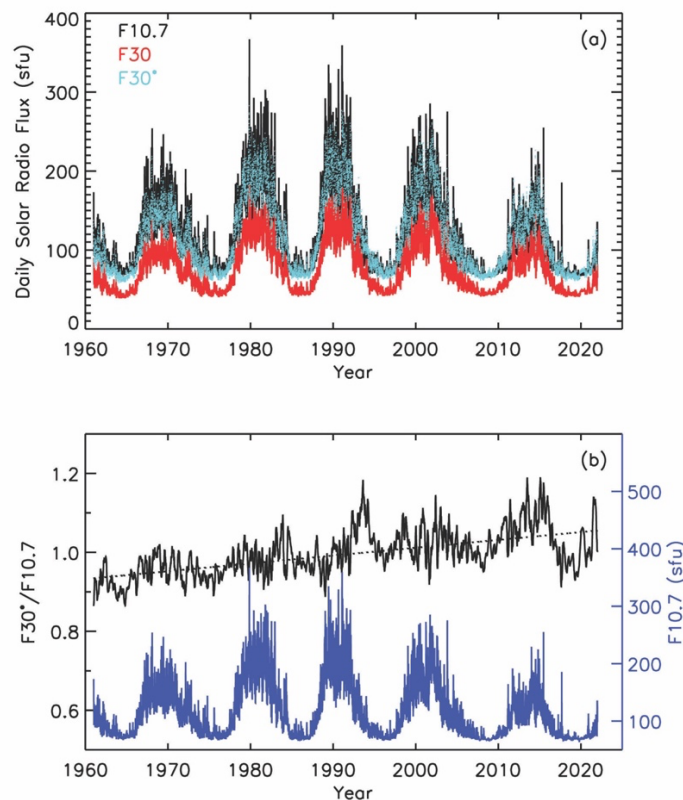
147 suitable for climatological studies of thermospheric density variations and trends, and for space
148 weather studies on time scales longer than 3 days.

149
150 *NASA GOLD Qeuv Data*

151 The GOLD instrument is onboard the SES-14 communication satellite, which was launched
152 on January 25, 2018. The satellite is located on a geostationary orbit at 47.5°W. The GOLD Far
153 Ultra-Violet (FUV) imager observes the Earth's FUV airglow at 134–162 nm, including the OI
154 135.6 nm and N2 Lyman-Birge-Hopfield (LBH) bands. We will use the current version of Qeuv
155 (L2 version 4; Correira et al., 2021) in this study. Qeuv ($\text{erg cm}^{-2} \text{s}^{-1}$) is a measure of solar extreme
156 ultraviolet (EUV) energy flux into the I-T system in the wavelength band from 1 to 45 nm, derived
157 from the GOLD FUV observations (see Eastes et al., 2020, for more details).

158
159 **3. Results**

160 Figure 1a shows daily solar radio fluxes F10.7 (in black), F30 (in red), and F30* (the scaled
161 F30, in cyan) from 1961–2019. Figure 1b shows the ratio of the 81-day averaged F30* and F10.7
162 and its linear fit. It is evident that during this period, F30* increased with respect to F10.7. Mursula
163 et al. (2024) conducted a detailed analysis of the long-term evolution of radio fluxes, showing that
164 both F30 and F15 increased with respect to F10.7 from the 1960s to the 2010s (see Figure 5 of
165 Mursula et al., 2024). They also found that F30 increases with respect to F15 (measured by the
166 same instrument as F30), which excludes the possibility that the relative drift of F10.7 and F30 is
167 due to an instrumental defect.



168
169 Figure 1: (a) Black: daily solar radio fluxes F10.7; red: F30; cyan: F30* (scaled F30, $F30^* =$
170 $1.554 \times F30 - 1.6$). (b) Black: ratio of the 81-day averaged F30* and F10.7; black dotted line:
171 linear fit to the ratio; blue: daily F10.7 for reference.

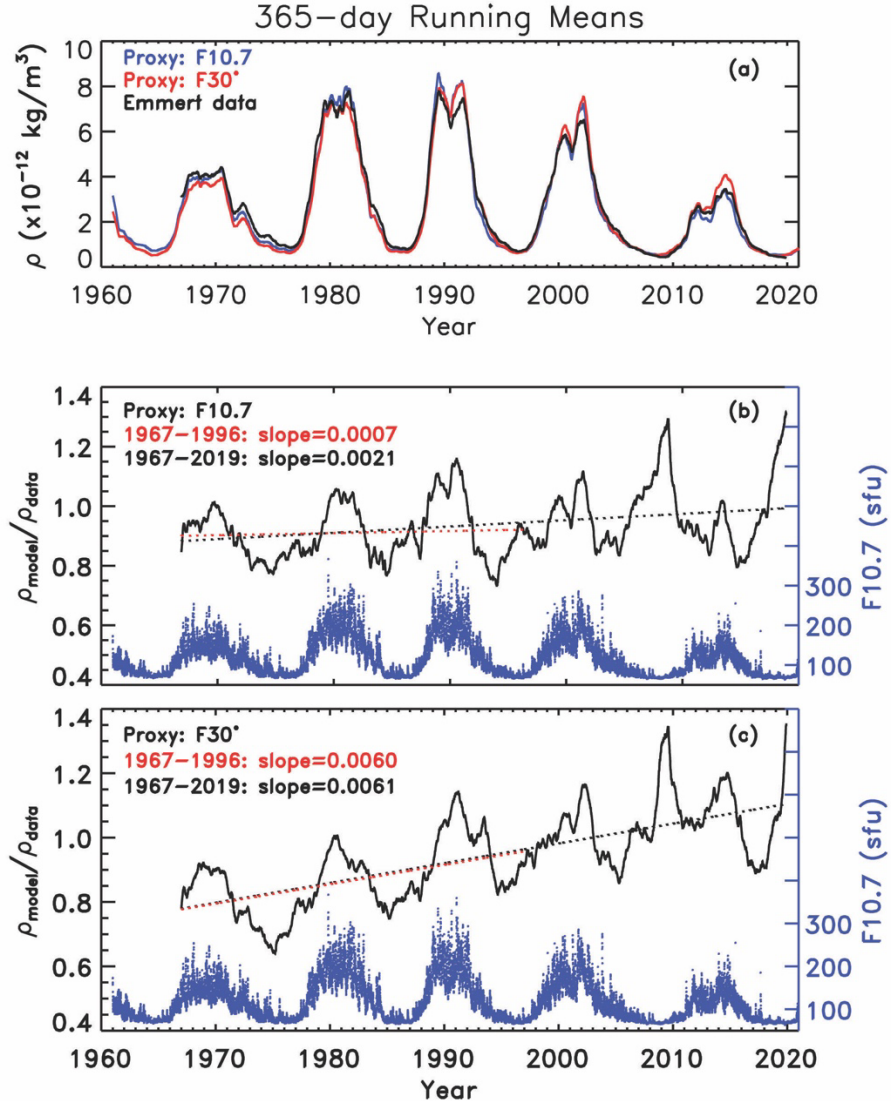
172
173 We conducted two model simulations using the global mean version of the NCAR TIME-
174 GCM model (Roble et al., 1987; Roble and Ridley, 1994). The two model simulations are the same
175 except that one simulation used the standard EUVAC solar proxy model (Richards et al., 1994)
176 for solar irradiance input, which uses the F10.7 flux, while in the other simulation we replaced the
177 F10.7 flux by the F30* flux in the EUVAC model. Figure 2a shows the 365-day running-mean of
178 daily global averaged mass density at 400 km (1961–2019 for the simulated densities, 1967–2019
179 for the satellite drag derived mass density): mass density derived from satellite drag data in black,
180 simulated mass density using the F10.7 flux in blue, and simulated mass density using the F30*
181 flux in red. The simulated densities reproduce closely the solar cycle variability of the
182 observational data. However, there are notable quantitative differences both during solar maximum
183 and minimum periods.

184
185 To better evaluate the difference between the simulated and observed mass densities, we
186 calculated the ratios of the simulated and observed mass densities. The mass density values are the
187 365-day running-mean of daily global averaged mass densities at 400 km from Figure 2a. Figure
188 2b shows the ratio of the mass densities using the F10.7 flux in simulation. The linear slope
189 ($k=0.0021$) for the entire period 1967–2019 is significantly larger than the linear slope ($k=0.0007$)
190 for the earlier period 1967–1996, indicating that there is a change in the linear relation between
191 mass density ratio and F10.7 around the minimum between cycles 22 and 23. ~~Note that t~~The F-test
192 statistics F for these two linear regressions are 1851 and 44, indicating that the linear fittings are
193 statistically significant (in F-test, if $F > 2.5$ then we can reject the null hypothesis). Note the upward
194 linear slope in the density ratio between simulated and orbit-derived mass density for the period
195 1967–2019 in Figures 2b and 2c, which will be discussed later. This slope does not describe the
196 long-term effect caused by increasing CO₂ concentrations. Both the simulated and orbit-derived
197 mass densities include the trend driven by the rising CO₂ level: the model simulations incorporate
198 time-varying CO₂ concentrations measured at the Mauna Loa Observatory (Qian et al., 2006), and
199 Emmert (2015) demonstrated that the height dependence of orbit-derived mass-density trends
200 agree with model simulations of the impact of increasing CO₂. The significantly larger slope (about
201 0.0021) of the F10.7 model for the longer period 1967–2019 arises because the F10.7 model is
202 unable to explain the very small density during the unusually low solar minima of 2008–2009 and
203 2019–2020 because of enhanced saturation of the F10.7 flux. This will be discussed further later.

204 This change of the linear relation between the density ratio and F10.7 after approximately
205 1996 in Figure 2b is consistent with the change of the slope of the linear relation between foF2
206 and F10.7 (see Figure 2 in Laštovička, 2019). Note also that, the observed density is used to
207 calculate the ratios of densities, to normalize the simulated densities for solar cycle variability.
208 From 1960s to about 1996, the ratio fluctuated roughly in phase with the solar cycle, indicating
209 that the model relatively overestimates the mass density during solar maxima but underestimates
210 it during solar minima. Since the simulated densities using F10.7 (F30*) reflect solar irradiance
211 energy deposition represented by F10.7 (F30*), the slope between the simulated densities
212 normalized by the observed densities and time can reveal how well F10.7 and F30* serve as
213 proxies for solar irradiance energy input for the thermosphere over this several decades period.

214
215 Figure 2c shows the ratio of the simulated mass density to the drag derived mass density from
216 1967 to 2019, using F30* in simulation. The linear slope of the ratio throughout the whole period
217 from 1967 to 2019 (0.0061) is almost unchanged from the linear slope for the earlier period of

218 1967 – 1996 (0.0060). Note that the F-test statistics for these two linear regressions are 17809 and
 219 3254, indicating that the linear fittings are statistically significant. The constancy of slopes is
 220 consistent with Laštovička & Burešova (2023), who demonstrated that the dependence of the
 221 yearly averaged foF2 on F10.7 is significantly steeper in 1996–2014 than in 1976–1995, whereas
 222 for F30 the two intervals provide no significant difference.



223
 224 Figure 2: (a) 365-day running means of the daily and globally averaged mass density at 400 km.
 225 Black: mass density derived from satellite drag data; blue: simulated mass density using F10.7 as
 226 a solar EUV proxy; red: simulated mass density using F30* as a solar EUV proxy. (b) Solid black:
 227 mass density ratio of the simulated density using F10.7 as a solar EUV proxy to the density derived
 228 from satellite drag; red dotted line: linear fit to the mass density ratio from 1967–1996; black dotted
 229 line: linear fit to the mass density ratio from 1967–2019; blue: daily F10.7 for reference. (c) Same
 230 as (b), but for the case with the simulated mass density using F30* as a solar EUV proxy.
 231

232 The change of the linear slope of the density ratio after about 1996 shown in Figure 2b can be
 233 explained by increased saturation of the F10.7 flux during the extremely low solar activity minima
 234 of 2008–2009 and 2019–2020. It is known that the F10.7 flux does not decrease below a certain

235 minimum value of about 67, which comes from thermal emission of radio waves (see Tapping and
236 Morgan, 2017) even when solar EUV activity continues to decrease. Figure 2b shows that, during
237 these two extended solar minima, the simulated mass density breaks the pattern of underestimating
238 mass density at solar minima. Rather, it significantly overestimates the mass density compared to
239 the observed density. This happens because of the increased saturation of the F10.7 flux during
240 these two extended minima when solar activity was very low during a longer time than in earlier
241 minima. On the other hand, the observed mass density continues to decrease as the actual solar
242 EUV activity continues to decline. The overestimation of the simulated mass density at these two
243 solar minima leads to the change of the density ratio slope after solar cycle 22 seen in Figure 2b.
244 Note also that the ratio in Figure 2b always reaches its cycle minimum in the declining phase rather
245 than at the exact minimum, where it always has a local maximum, even during the minima before
246 the two extended minima. This indicates that saturation has occurred at all solar minima, but has
247 remained unnoticed during the earlier, shorter minima and became evident only during the longer
248 and weaker minima of the 2000s and 2010s (e.g., Elias, 2023).

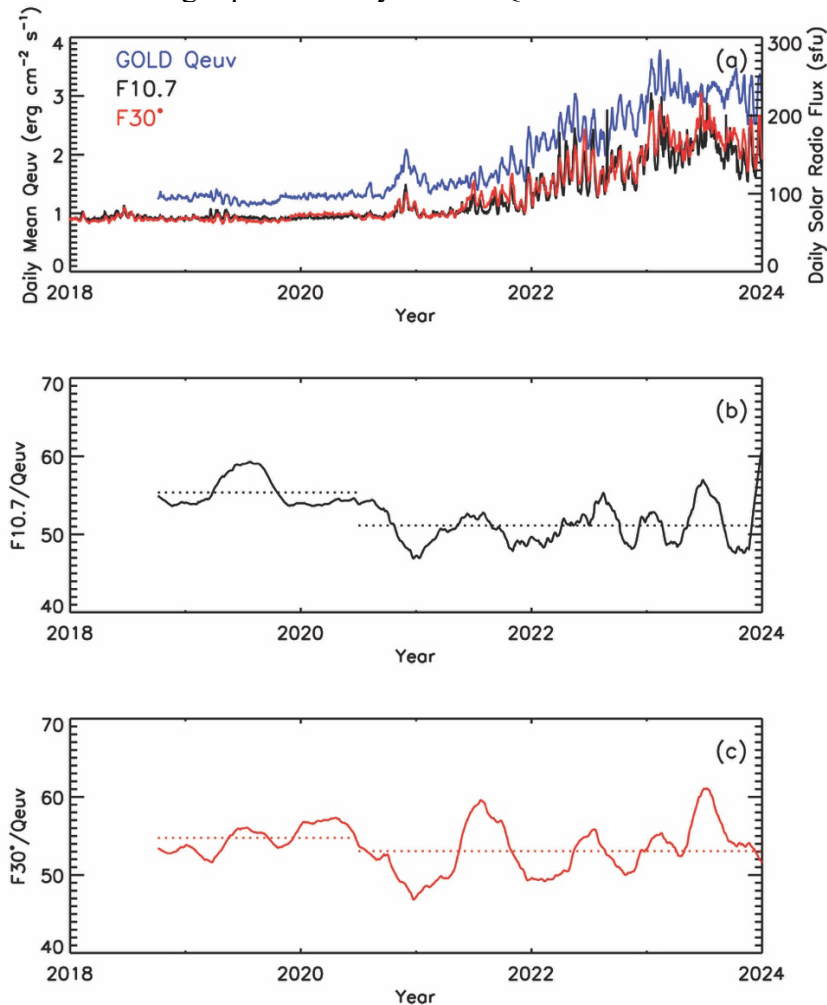
249
250 This raises a question: why the linear slope of the density ratio in Figure 2c does not show a
251 similar clear change as the ratio in Figure 2b? Note first that the ratio in Figure 2c also depicts high
252 maxima during the two extended minima in 2008–2009 and 2019–2020, while the cycle maxima
253 in earlier cycles were found at solar maxima, similarly to Figure 2b. However, in contrary to Figure
254 2b, the ratio in Figure 2c has an upward slope during the whole period depicted in Figure 2c. It is
255 clear that this increasing trend is not due to the increased saturation during the last two minima.
256 This raises another question: why the density ratio for the simulated density using F30* (Figure
257 2c) has a continuously upward slope, whereas the ratio using F10.7 (Figure 2b) is nearly flat during
258 the first part of the studied interval in solar cycles 20, 21, and 22?

259
260 Recall that the solar irradiance input for the NCAR global mean model is via EUVAC, which
261 is based on the F10.7 flux (Richards et al., 1994). The period from the peak of the Modern
262 Maximum in solar cycle 19 through solar cycle 22 does not have extended (extremely low or long)
263 solar minima, so the ratio of the simulated density and the observed density fluctuates around a
264 constant without a trend. As discussed above, the linear slope of the density ratio in Figure 2b
265 changed after solar cycle 22 because of increased saturation of the F10.7 flux during the extended
266 solar minima of 2008–2009 and 2019–2020. This increased the minimum-time ratio above one,
267 which made the linear slope turn upward. In the case of the ratio using F30* (Figure 2c), since F30
268 increases with respect to F10.7 during the whole period (Mursula et al., 2024; see also Figure 1b),
269 the simulated mass density using F30* also increases in time compared to the simulation using
270 F10.7, thus producing an upward slope in the F30* ratio which persists during the whole period.
271 The increased saturation during the extended minima affects also F30*, but its effect on the slope
272 of the F30* ratio in Figure 2c remains rather small. This explains why the slope of the F30* model
273 to observation ratio in Figure 2c depicted no significant change but, rather, remained fairly stable
274 during the whole period of 1967–2019.

275
276 The linear relation between thermospheric mass density and F30* remains closely the same
277 during the whole studied period of 1967–2019, but it has an upward slope. However, for an
278 optimum proxy of solar irradiance in upper atmosphere models, the slope of the density ratio
279 should be zero, as seen for F10.7 until 1996 (Figure 2b), at most only fluctuating around 1. To

280 achieve this goal, a solar proxy model similar to the EUVAC needs to be developed based on the
 281 F30 flux. However, this calibration project is beyond the scope of this paper.

282
 283 Next, we use another new thermospheric dataset to verify the above findings. Figure 3a shows
 284 the GOLD daily mean Q_{EUV} data from October 2018 to 2023 in blue, the daily F10.7 flux in black,
 285 and the daily F30* flux in red. Q_{EUV} is derived from NASA GOLD FUV airglow data and
 286 represents the integrated solar EUV energy between 1 and 45 nm incident on the upper atmosphere
 287 (Correira et al., 2021). Figure 3b shows the ratio of the 81-day averaged F10.7 flux to the 81-day
 288 averaged Q_{EUV} in black from October 2018 to December 2023. Figure 3b shows that the F10.7 to
 289 Q_{EUV} ratio is unstable in time, being consistently at a larger level from the start of the ratio in
 290 October 2018 to the first half of 2020 (average ratio of 55) compared to the rest of the time interval
 291 when the ratio oscillates at a considerably lower average level (average ratio of 51). The first
 292 interval is exactly the solar minimum period of the later extended minimum when solar activity
 293 was extremely low. This verifies that the observed F10.7 flux during this minimum time is larger
 294 than the actual solar EUV forcing represented by GOLD Q_{EUV} .



295
 296 Figure 3: (a) Blue: GOLD daily mean Q_{EUV} ; black: daily F10.7; red: daily F30*. (b) Black solid
 297 line: ratio of the 81-day averaged F10.7 and Q_{EUV} ; black dotted lines: the mean ratios for the
 298 periods of the extended minimum (late 2018 to first half of 2020) and after the extended minimum
 299 (second half of 2020 to 2023). (c) Red solid line: ratio of the 81-day averaged F30* and Q_{EUV} ; red

300 dotted lines: the mean ratios for the periods of the extended minimum (late 2018 to first half of
301 2020) and after the extended minimum (second half of 2020 to 2023).

302
303 On the other hand, the ratio between the 81-day average F30* and the 81-day averaged Qeuv
304 in Figure 3c remains more stable in time. The mean value of this ratio during the first interval from
305 October 2018 to June 2020 (average ratio of 55) is somewhat larger than its mean during the latter
306 period (average ratio of 53). Accordingly, this ratio was raised by a factor of about 4% during the
307 extended minimum. This is considerably less than for the F10.7 flux (a factor of about 8%), which
308 supports the above result that the F30 flux is more suitable to be used as a solar EUV proxy in
309 thermospheric modeling. Since the effect of increased saturation to F30* during the extended
310 minima is rather small, its effect on slope of the F30* ratio in Figure 2c also remains rather small,
311 explaining why the slope of the F30* model to observation ratio in Figure 2c depicted no
312 significant change but, rather, remained fairly stable in time. This gives further evidence that F30
313 can more consistently represent the solar EUV energy deposition in the thermosphere better than
314 F10.7 during the last several decades of weakening solar activity.

315 316 **4. Discussion**

317 The recent solar minima in 2008 – 2009 and in 2019 – 2020, together with the intervening low
318 solar cycle 24, may reproduce a similar centennial solar minimum as found earlier for 1810–1830
319 and 1900–1910 (Feynman and Ruzmaikin, 2014). They suggested that such long minima are
320 minima related to Gleissberg cyclicity, a roughly 100-year quasi-periodic variation observed in
321 sunspot activity, in the solar wind, in geomagnetic activity, and throughout the heliosphere. The
322 Modern Maximum is only the most recent repetition of this periodicity, and the last 60 years
323 studied here, from the maximum of solar cycle 19 to the extended minimum in 2008-2009, form
324 the decay phase of this latest Gleissberg cycle. Since then, with cycle 25 exceeding the activity of
325 cycle 24, the Sun may be slowly transitioning into the growth phase of the next Gleissberg cycle,
326 the Future Maximum (Mursula, 2023).

327
328 A smaller fraction of solar radio flux is generated in sunspots, while a larger fraction is
329 produced in active regions (chromospheric plages) (Schonfeld et al., 2015). The frequency of radio
330 waves produced in the active regions depends on local plasma density. Shorter (longer) radio
331 waves are produced in more dense (rarefied, respectively) regions at a somewhat lower (higher)
332 altitude in the solar atmosphere. As argued by Mursula et al. (2024), the observed relative increase
333 of the flux of longer radio waves with respect to shorter radio waves can be explained by a less
334 rapid cooling of the longer waves due to a larger volume compression in the canopy structure of
335 solar magnetic field lines. This evolution of the solar radio fluxes and other solar parameters
336 (Mursula et al., 2024) indicates that, as the overall solar activity weakens during the decay of the
337 Modern Maximum, the solar parameters being produced at different mean heights of solar
338 atmosphere vary slightly but systematically differently.

339
340 So, how will these relations evolve in the future? As solar cycles will very likely start growing
341 again, the extended minima will turn more normal, and saturation will decrease. Consequently, the
342 relation of F10.7 with the EUV flux (and thermospheric mass density) will be temporally more
343 stable, and the current EUVAC model based on F10.7 can be used. However, it is expected
344 (Mursula et al., 2024) that, with increasing solar activity, the mutual relation of F10.7 and F30 will
345 very likely be opposite to that seen during the decay of the Modern Maximum. Then F30 would

346 decrease with respect to F10.7. In view of these interesting forecasts, we believe that it is necessary
347 to continue evaluating these relations between thermospheric-ionospheric parameters and radio
348 fluxes during the coming decades.

349

350 **5. Conclusions**

351 In this study we found the following results:

352 (1) Minimum-time saturation of the F10.7 flux as a solar EUV proxy remained unnoticed until
353 it increased and became evident during the extended solar minima in 2008–2009 and 2019–2020.
354 Models based on the F10.7 flux have overestimated the solar irradiance energy deposition in the
355 thermosphere because of this increased saturation. We demonstrated this in a change of the linear
356 relation between the modeled and observed thermospheric density during the last 60 years, when
357 solar activity is weakening in the decay of the Modern Maximum.

358 (2) F30 increases with respect to F10.7 during this period, so the simulated mass density using
359 F30* also increases in time compared to the simulation using F10.7, thus producing an upward
360 slope in the ratio of F30*-modeled and observed densities. Increased saturation during the
361 extended minima affects also to F30*, but its effect on slope of the F30* ratio remains rather small.
362 Consequently, the linear relation between thermospheric mass density simulated using F30* and
363 observed density remains stable during the whole period of 1967–2019. This explains the earlier
364 finding that F30 correlates better with several ionospheric and thermospheric parameters than
365 F10.7 during the last decades.

366 (3) However, because the F30 flux increases relative to the F10.7 flux from the 1960s until
367 2010s (Mursula et al., 2024) and because the thermospheric models are calibrated to use the F10.7
368 flux, the models using F30 correlated to F10.7 show a continuous increase which need to be
369 removed by recalibrating models to use the F30 index.

370

371 Future work includes:

372 (1) Developing a solar proxy model, similar to the EUVAC, but based on the F30 flux. This
373 would enable using F30 as a long-term consistent solar irradiance proxy in upper atmosphere and
374 whole atmosphere models.

375 (2) Continuing to evaluate how the F10.7 and F30 fluxes will succeed as solar EUV proxies
376 for the thermosphere and ionosphere in the future, during the expected increase of solar activity in
377 future solar cycles (Mursula, 2023). This entails, for example, continued efforts in evaluating the
378 relation between different thermospheric-ionospheric parameters and solar radio fluxes.

379

380 **Author contribution** LQ carried out numerical model simulations and model-data comparisons.
381 KM analyzed solar radio fluxes. LQ and KM decided on the contents and key points of the
382 manuscripts.

383

384 **Acknowledgments** This study is supported by NASA Grants 80NSSC20K0189,
385 80NSSC19K0278, 80NSSC19K0835, and 80NSSC21K1315. The National Center for
386 Atmospheric Research is a major facility sponsored by the National Science Foundation under
387 Cooperative Agreement No. 1852977. We would like to acknowledge high-performance
388 computing support from Cheyenne (doi: 10.5065/D6RX99HX) provided by NCAR's
389 Computational and Information Systems Laboratory, sponsored by the National Science
390 Foundation.

391

392 **Competing Interests** Liying Qian is one of the topical editors for the special issue “Long-term
393 trends in the stratosphere–mesosphere–thermosphere–ionosphere system.”
394

395 **Code/Data Availability**

396 Solar radio flux data are available from the Collecte Localisation Satellites (CLS) website at
397 <https://spaceweather.cls.fr/services/radioflux/>. Thermosphere mass density dataset is available at
398 https://map.nrl.navy.mil/map/pub/nrl/orbit_derived_density/. GOLD Qeuv data from 10/5/2018
399 onward is available at <https://gold.cs.ucf.edu/data/search/>. The NetCDF and IDL sav data used to
400 produce the Figures in this paper, including both model simulation and observational data (Qian,
401 2024), are available at National Center for Atmospheric Research Geoscience Data Exchange
402 Repository via <https://doi.org/10.5281/zenodo.13909713>.
403

404 **References**

- 405
- 406 Bruinsma, S.L., N. Sánchez-Ortiz, E. Olmedo & N. Guijarro (2012) Evaluation of the DTM-2009
407 thermosphere model for benchmarking purposes, *Journal of Space Weather and Space Climate*,
408 <http://dx.doi.org/10.1051/swsc/2012005>
- 409 Bruinsma, S (2015). The DTM-2013 thermosphere model. *J. Space Weather Space Clim.*, 5 (27),
410 A1, 2015, DOI: 10.1051/swsc/2015001.
- 411 Correira, J., Evans, J. S., Lumpe, J. D., Krywonos, A., Daniell, R., Veibell, V., et al. (2021).
412 Thermospheric composition and solar EUV flux from the Globalscale Observations of the
413 Limb and Disk (GOLD) mission. *Journal of Geophysical Research: Space Physics*, 126,
414 e2021JA029517. <https://doi.org/10.1029/2021JA029517>
- 415 Danilov, A.D., Berbeneva, N.A (2024), Dependence of foF2 on Solar Activity Indices Based on
416 the Data of Ionospheric Stations of the Northern and Southern Hemispheres. *Geomagn. Aeron.*
417 64, 224–234 (2024). <https://doi.org/10.1134/S0016793223601035>
- 418 Dudok de Wit, T. and S. Bruinsma (2017), The 30 cm radio flux as a solar proxy for thermosphere
419 density modelling, *J. Space Weather Space Clim.*, 7, A9 (2017), DOI: 10.1051/swsc/2017008.
- 420 Eastes, R. W., McClintock, W. E., Burns, A. G., Anderson, D. N., Andersson, L., Aryal, S., et al.
421 (2020). Initial Observations by the GOLD Mission. *Journal of Geophysical Research: Space*
422 *Physics*, 125(7), e27823. <https://doi.org/10.1029/2020JA027823>
- 423 Elias, A. G., Martinis, C. R., de Haro Barbas, B. F., Medina, F. D., Zossi, B. S., Fagre, M., and
424 Duran, T. (2023). Comparative analysis of extreme ultraviolet solar radiation proxies during
425 minimum activity levels. *Earth Planet. Phys.*, 7(5), 540–547. DOI: 10.26464/epp2023050
- 426 Emmert, J. T. (2015). Altitude and solar activity dependence of 1967–2005 thermospheric density
427 trends derived from orbital drag, *J. Geophys. Res. Space Physics*, 120, 2940–2950,
428 [doi:10.1002/2015JA021047](https://doi.org/10.1002/2015JA021047).
- 429 Emmert, J. T., Dhadly, M. S., & Segerman, A. M. (2021). A globally averaged thermospheric
430 density data set derived from two-line orbital element sets and special perturbations state
431 vectors. *Journal of Geophysical Research: Space Physics*, 126, e2021JA029455.
432 <https://doi.org/10.1029/2021JA029455>
- 433 Fang, T.-W., R. Akmaev, R. A. Stoneback, T. Fuller-Rowell, H. Wang, and F. Wu (2016), Impact
434 of midnight thermosphere dynamics on the equatorial ionospheric vertical drifts, *J. Geophys.*
435 *Res. Space Physics*, 121, 4858–4868
- 436 Fang, T.-W., T. Fuller-Rowell, V. Yudin, T. Matsuo, R. Viereck (2018), Quantifying the sources
437 of ionosphere day-to-day variability, *J. Geophys. Res. Space Physics*, 123.
- 438 Feynman, J., and A. Ruzmaikin (2014), The Centennial Gleissberg Cycle and its association with
439 extended minima, *J. Geophys. Res. Space Physics*, 119, 6027–6041,
440 [doi:10.1002/2013JA019478](https://doi.org/10.1002/2013JA019478).
- 441 Fuller-Rowell, T. J., and D. Rees (1980), A three-dimensional, time-dependent model of the
442 thermosphere, *J. Atmos. Sci.*, 37, 2545-- 2567.
- 443 Fuller-Rowell, T. J., R. Akmaev, F. Wu, A. Anghel, N. Maruyama, D. N. Anderson, M. V.
444 Codrescu, M. Iredell, S. Moorthi, H.-M. Juang, Y.-T. Hou, and G. Millward (2008), Impact of
445 terrestrial weather on the upper atmosphere, *Geophys. Res. Lett.*, 35, L09808.
- 446 Lastovicka, J. (2019). Is the relation between ionospheric parameters and solar proxies stable?
447 *Geophysical Research Letters*, 46, <https://doi.org/10.1029/2019GL085033>
- 448 Laštovička, J., & Burešová, D. (2023). Relationships between foF2 and various solar activity
449 proxies. *Space Weather*, 21, e2022SW003359. <https://doi.org/10.1029/2022SW003359>

450 Liu, H.-L., Bardeen, C. G., Foster, B. T., Lauritzen, P., Liu, J., Lu, G., . . . Wang, W. (2018).
451 Development and validation of the Whole Atmosphere Community Climate Model with
452 thermosphere and ionosphere extension (WACCM-X 2.0). *Journal of Advances in Modeling*
453 *Earth Systems*, 10, 381–402. <https://doi.org/10.1002/2017MS001232>.

454 Millward, G. H., I. C. F. Müller-Wodrag, A. D. Aylward, T. J. Fuller-Rowell, A. D. Richmond,
455 and R. J. Moffett (2001), An investigation into the influence of tidal forcing on F region
456 equatorial vertical ion drift using a global ionosphere-thermosphere model with coupled
457 electrodynamics, *J. Geophys. Res.*, 106, 24,733 -- 24,744, doi:10.1029/2000JA000342.

458 Mursula, K. (2023). Hale cycle in solar hemispheric radio flux and sunspots: Evidence for a
459 northward shifted relic field, *Astron. Astrophys.*, 674, A182, [https://doi.org/10.1051/0004-](https://doi.org/10.1051/0004-6361/202345999)
460 [6361/202345999](https://doi.org/10.1051/0004-6361/202345999).

461 Mursula, K., A. A. Pevtsov, T. Asikainen, I. Tähtinen, and A. Yeates (2024). Transition to a weaker
462 Sun: Changes in the solar atmosphere during the decay of the Modern maximum, *Astron.*
463 *Astrophys.*, 685, A170, <https://doi.org/10.1051/0004-6361/202449231>.

464 Qian, L., R. G. Roble, S. C. Solomon, and T. J. Kane (2006), Calculated and observed climate
465 change in the thermosphere, and a prediction for solar cycle 24, *Geophys. Res. Lett.*, 33,
466 L23705, doi:10.1029/2006GL027185.

467 Qian, L., A. G. Burns, B. A. Emery, B. Foster, G. Lu, A. Maute, A. D. Richmond, R. G. Roble, S.
468 C. Solomon, and W. Wang (2014), The NCAR TIE-GCM: A community model of the coupled
469 thermosphere/ionosphere system, in *Modeling the Ionosphere-Thermosphere System*, AGU
470 Geophysical Monographs. <https://doi.org/10.1002/9781118704417.ch7>

471 Qian, L. (2024). Evaluating F10.7 and F30 Radio Fluxes as Long-Term Solar Proxies of Energy
472 Deposition in the Thermosphere [Dataset]. UCAR/NCAR Data Exchange Repository via
473 <https://doi.org/10.5281/zenodo.13909713>.

474 Richards, P. G., J. A. Fennelly, and D. G. Torr (1994), EUVAC: A solar EUV flux model for
475 aeronomic calculations, *J. Geophys. Res.*, 99, 8981.

476 Richmond, A. D., E. C. Ridley, and R. G. Roble (1992), A thermosphere/ionosphere general
477 circulation model with coupled electrodynamics, *Geophys. Res. Lett.*, 19, 601.

478 Ridley, A. J., Deng, Y., and Toth, J. (2006), The global ionosphere–thermosphere model, *Journal*
479 *of Atmospheric and Solar-Terrestrial Physics* 68, 839–864.

480 Roble, R. G., E. C. Ridley, and R. E. Dickinson (1987), On the global mean structure of the
481 thermosphere, *J. Geophys. Res.*, 92, 8745.

482 Roble, R. G., and E. C. Ridley (1994), Thermosphere-ionospheremesosphere-electrodynamics
483 general circulation model (TIME-GCM): Equinox solar min simulations, 30– 500 km,
484 *Geophys. Res. Lett.*, 21, 417.

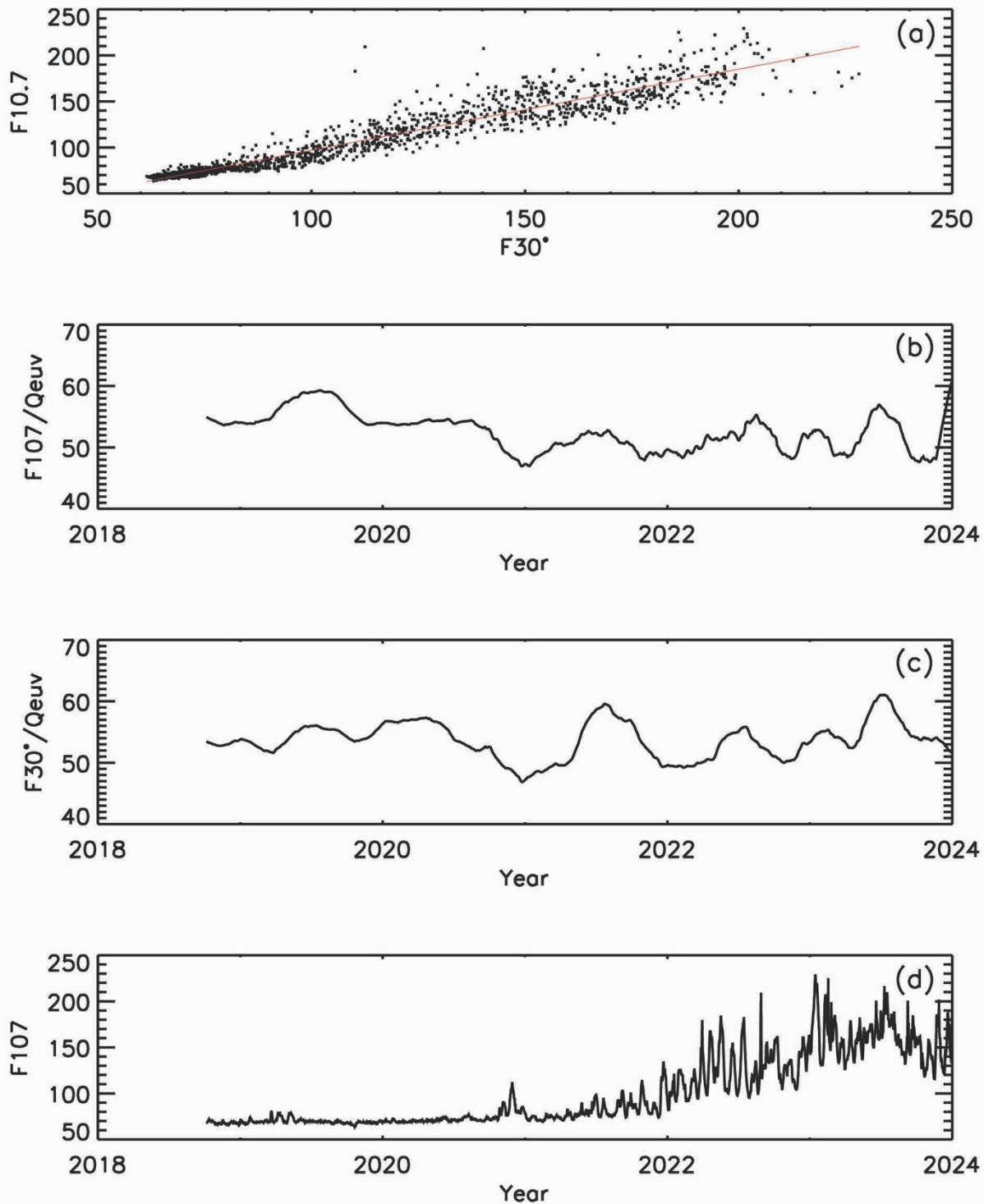
485 Roble, R. G. (1995), Energetics of the mesosphere and thermosphere, in *The Upper Mesosphere*
486 *and Lower Thermosphere: A Review of Experiment and Theory*, *Geophys. Monogr. Ser.*, vol.
487 87, edited by R. M. Johnson and T. L. Killeen, p. 1, AGU, Washington, D. C.

488 Schonfeld, S. J., White, S. M., Henney, C. J., Arge, C. N., and McAteer, R. T. J. (2015). Coronal
489 Sources of the Solar F10.7 Radio Flux, *Astrophys. J.*, 808, 29, doi:10.1088/0004-
490 637X/808/1/29.

491 Shimojo, M., K. Iwai, A. Asai, S. Nozawa, T. Minamidani, and M. Saito, 2017. Variation of the
492 Solar Microwave Spectrum in the Last Half Century. *Astrophys. J.*, 848(1), 62. [10.3847/1538-](https://doi.org/10.3847/1538-4357/aa8c75)
493 [4357/aa8c75](https://doi.org/10.3847/1538-4357/aa8c75), 1709.03695. 2.2

494 Solomon, S. C., and L. Qian (2005), Solar extreme-ultraviolet irradiance for general circulation
495 models, *J. Geophys. Res.*, 110, A10306, doi:10.1029/2005JA011160.

496 Tapping, K. and C. Morgan (2017), Changing Relationships Between Sunspot Number, Total
497 Sunspot Area and F10.7 in Cycles 23 and 24, Solar Phys (2017) 292:73, DOI
498 10.1007/s11207-017-1111-6
499



500
 501
 502
 503
 504

Figure R1: (a) Scatter plot between F10.7 and F30*; (b) ratio of the 81-day averaged F10.7 and Quuv; (c) ratio of the 81-day averaged F30* and Quuv; (d) daily F10.7.